









RESEARCH ARTICLE | DECEMBER 18 2023

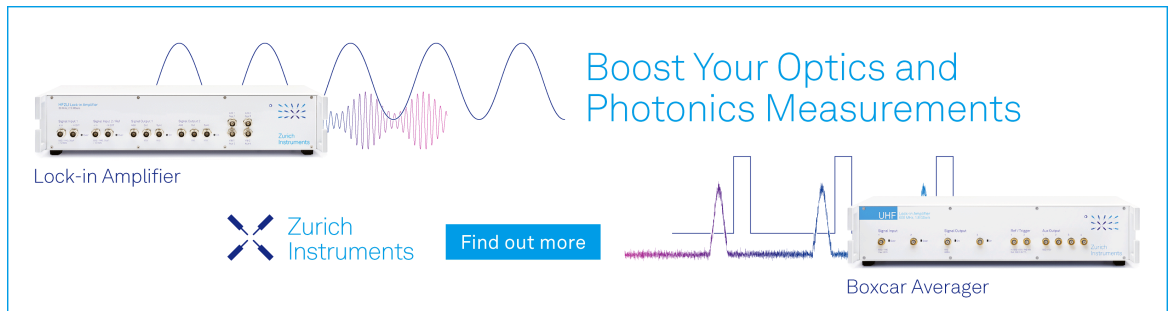
Experimental and numerical studies on the thermal nonequilibrium behaviors of CO with Ar, He, and H₂

Dong He ; Qizhen Hong ; Fei Li ; Quanhua Sun  ; Ting Si  ; Xisheng Luo 




J. Chem. Phys. 159, 234302 (2023)

<https://doi.org/10.1063/5.0176176>



Boost Your Optics and
Photonics Measurements

Lock-in Amplifier

 Zurich
Instruments

[Find out more](#)

Boxcar Averager

Experimental and numerical studies on the thermal nonequilibrium behaviors of CO with Ar, He, and H₂

Cite as: J. Chem. Phys. 159, 234302 (2023); doi: 10.1063/5.0176176

Submitted: 11 September 2023 • Accepted: 24 November 2023 •

Published Online: 18 December 2023



View Online



Export Citation



CrossMark

Dong He,^{1,2}  Qizhen Hong,²  Fei Li,²  Quanhua Sun,^{2,3,a)}  Ting Si,^{1,2,a)}  and Xisheng Luo^{1,2} 

AFFILIATIONS

¹ Deep Space Exploration Laboratory, Department of Modern Mechanics, University of Science and Technology of China, Hefei 230026, People's Republic of China

² State Key Laboratory of High Temperature Gas Dynamics, Institute of Mechanics, Chinese Academy of Sciences, Beijing 100190, People's Republic of China

³ School of Engineering Science, University of Chinese Academy of Sciences, Beijing 100049, People's Republic of China

^{a)} Authors to whom correspondence should be addressed: qsun@imech.ac.cn and tsi@ustc.edu.cn

ABSTRACT

The time-dependent rotational and vibrational temperatures were measured to study the shock-heated thermal nonequilibrium behaviors of CO with Ar, He, and H₂ as collision partners. Three interference-free transition lines in the fundamental vibrational band of CO were applied to the fast, *in situ*, and state-specific measurements. Vibrational relaxation times of CO were summarized over a temperature range of 1110–2820 K behind reflected shocks. The measured rotational temperature instantaneously reached an equilibrium state behind shock waves. The measured vibrational temperature experienced a relaxation process before reaching the equilibrium state. The measured vibrational temperature time histories were compared with predictions based on the Landau–Teller model and the state-to-state approach. The state-to-state approach treats the vibrational energy levels of CO as pseudo-species and accurately describes the detailed thermal nonequilibrium processes behind shock waves. The datasets of state-specific inelastic rate coefficients of CO–Ar, CO–He, CO–CO, and CO–H₂ collisions were calculated in this study using the mixed quantum-classical method and the semiclassical forced harmonic oscillator model. The predictions based on the state-to-state approach agreed well with the measured data and nonequilibrium (non-Boltzmann) vibrational distributions were found in the post-shock regions, while the Landau–Teller model predicted slower vibrational temperature time histories than the measured data. Modifications were applied to the Millikan–White vibrational relaxation data of the CO–Ar and CO–H₂ systems to improve the performance of the Landau–Teller model. In addition, the thermal nonequilibrium processes behind incident shocks, the acceleration effects of H₂O on the relaxation process of CO, and the characterization of vibrational temperature were highlighted.

Published under an exclusive license by AIP Publishing. <https://doi.org/10.1063/5.0176176>

I. INTRODUCTION

The fast flow inside the combustor of a scramjet is expected to be in a state of thermal nonequilibrium considering its short resident time. Previous numerical studies^{1,2} have illustrated that flame ignition and stabilization in supersonic combustion chambers are affected by the thermal nonequilibrium effects of high-temperature gases. CO is a key intermediate in the combustion process of hydrocarbon fuels. The behavior of CO formation and consumption is closely related to heat release and carbon conversion. In addition, predicting and managing heat transfer during the entry process of

missions to Mars and Venus is a crucial prerequisite for deep space exploration. The atmosphere of Mars and Venus is quickly decomposed into CO, O₂, and other species during the entry process of Mars and Venus missions. Previous studies^{3–7} have indicated that radiative heating during the entry process of the mission of these two planets is mainly from the CO fourth positive band and that the rovibrational states of nonequilibrium CO profoundly impact the intensity of radiative heating. Therefore, the rovibrational nonequilibrium characteristics of CO are closely related to research including supersonic combustion and deep space exploration. Argon is a commonly used diluent gas in shock-tube experiments to diminish

nonideal effects, including incident shock attenuation, boundary layer growth, and shock bifurcation. Helium and hydrogen are commonly used light gases to accelerate the vibrational relaxation process of CO in laser absorption measurements.^{8,9} In addition, H₂ is a key intermediate generated from H-abstraction reactions during hydrocarbon combustion,¹⁰ and the internal energy transfer (e.g., vibration–translation and vibration–vibration–translation) between CO and H₂ widely exists in supersonic combustion flow fields. Such examples have motivated us to take up the current study with a focus on the vibrational relaxation process in mixtures of CO with Ar, He, and H₂ as collision partners.

Laser interferometry¹¹ and gas emission¹² are the commonly used methods to measure the vibrational relaxation times of high-temperature gases behind shock waves. The former method indirectly measures the gas vibrational relaxation times by obtaining the density change information based on the change of interference fringes behind incident shock waves. The latter obtains the relaxation times of shock-heated high-temperature gases by measuring the time histories of emission signals in the specific spectral band. This method can obtain the emission information in specific spectral bands of high-temperature gases, thus providing an effective way to study the vibrational relaxation process based on different spectral bands. Many research groups used the above-mentioned methods to study the vibrational relaxation process of shock-heated high-temperature gases.^{13–19} In addition, multiple experimental studies of CO dissociation kinetics in shock tubes have been reported in the literature.^{20–23} Matthews¹³ and Millikan¹⁴ measured the vibrational relaxation times of high-temperature CO gas behind shock waves and studied the effects of different additives (H₂, N₂, O₂, CO₂, He, Ne, and Kr) on the thermal nonequilibrium process of CO. However, only one characteristic parameter, vibrational relaxation time, was measured in these studies. Time-resolved measurements of the nonequilibrium parameters are expected to provide more valuable data for studies on thermal nonequilibrium effects. Tunable diode laser absorption spectroscopy (TDLAS) is a highly selective and nonintrusive technique for accurately measuring temperature and species-concentration time histories with high time resolution.^{24,25} This technique has been widely used in multiparameter measurements during fuel reaction behind reflected shock waves.^{26–29} Compared to laser interferometry and gas emission, the TDLAS technique offers the prospect for fast, *in situ*, time-resolved, and quantum-state-specific measurements of multiple temperatures (translation, rotation, and vibration) and vibrational relaxation times by probing the individual energy levels of the target species. This technique has been applied to highly selective measurements of rotational and vibrational temperatures (simplified as T_{rot} and T_{vib} , respectively) of shock-heated thermal nonequilibrium species, including CO, CO₂, O₂, and NO.^{30–35}

The kinetics shock tube can instantaneously heat and compress the gas mixture behind shock waves, which is favorable for research on thermochemical nonequilibrium effects of high-temperature gases, including gas vibrational relaxation, decomposition, and combustion. The high-temperature region behind reflected shock waves is not temporally constant and spatially homogeneous due to the nonideal gas-dynamic effects, including attenuation of incident shock and boundary layer growth. Previous studies^{9,36} have characterized temperature variation assuming

isentropic compression (or expansion). The authors of the work of He *et al.*^{8,9,37} and Pineda *et al.*³⁸ observed real thermodynamic states during fuel reaction and used the measured pressure as input in kinetics simulation to diminish gaps between experiments and simulations. The impact of nonideal effects on the vibrational temperature time histories and vibrational relaxation times of high-temperature gases is an interesting research topic worth studying.

In addition to experimental measurements, great efforts have been devoted to the theoretical modeling and numerical simulation of the high-temperature thermochemical nonequilibrium effects. In the widely used multi-temperature framework,³⁹ the population of each internal energy mode (translation, rotation, and vibration) is assumed to follow a Boltzmann distribution under a particular temperature. Specifically, for the well-known two-temperature (2-T) model,³⁹ the translational and rotational energy modes are described by temperature T_{tr} , and the vibrational energy is independently treated by temperature T_{vib} . The energy transfer between these temperature modes is of great importance to modeling thermochemical nonequilibrium flows. Landau and Teller⁴⁰ developed a theoretical model for evaluating the energy exchange between translational and vibrational energy modes, in which a vibrational relaxation time is defined to characterize the rate of relaxation.⁴¹ Subsequently, Millikan and White¹⁸ summarized the vibrational relaxation times of various systems based on a large number of measured data.

The 2-T model based on the Landau–Teller formula and Millikan–White vibrational relaxation time has been the main tool for simulating thermochemical nonequilibrium flows for decades.³⁹ However, the above model is not able to accurately describe the nonequilibrium (non-Boltzmann) distribution of vibrational energy states; thus, it is not universally applicable for studying a flow that is in a strong nonequilibrium state. Instead, many recent works have focused on the high-fidelity state-to-state (StS) approach,^{42–46} which treats each vibrational energy level as a pseudo-species and can represent the non-Boltzmann vibrational distribution function, and then describe the detailed evolution of these thermochemical nonequilibrium processes. Inelastic and reactive collision processes of molecular states are elementary reactions in StS kinetics. The rate coefficients of these StS processes are mostly obtained by either the theoretical models [such as the Schwartz–Slawsky–Herzfeld theory⁴⁷ and the forced harmonic oscillator (FHO) model⁴⁸] or more accurate molecular dynamics calculations (such as the Quasi-Classical Trajectory method⁴⁹ and the mixed Quantum-Classical method⁵⁰) based on the *ab initio* potential energy surface (PES). Due to the expensive computational time involved (to solve hundreds of internal energy states with thousands of hundreds of StS transition processes), previous applications of the StS approach have been mainly limited to simple zero- or one-dimensional geometries, such as heat bath, one-dimensional nozzle, and post-shock flows, mainly for air species.^{42–44,51–55} The StS approach is also used to describe the nonequilibrium plasma kinetics of reacting CO for gas discharges^{56,57} and the radiative CO flow behind shock waves.^{58,59} Recently, two-dimensional calculations, implementing full state-to-state kinetics, have been performed for hypersonic flows over spheres and double cones,^{60,61} leading to improved alignment with experimental data when compared to the traditional 2-T model. Moreover, recent attempts^{45,46} have aimed at

applying the StS approach to study the ignition of hydrogen–air and syngas–air mixtures under thermochemical nonequilibrium conditions. In the present work, the StS approach is applied to investigate the thermal nonequilibrium process of CO gas behind shock waves with the presence of different additives (Ar, He, and H₂). The new datasets of vibrational StS rate coefficients (available in the supplementary material, S1) of the collision between CO and additives are obtained using the mixed Quantum–Classical method and the FHO model. The predictions of the StS approach serve as a reference for evaluating and correcting the 2-T simulation results.

In this study, the time-dependent T_{rot} and T_{vib} were measured and the vibrational relaxation times were summarized in mixtures of CO with Ar, He, and H₂ as collision partners in a temperature range of 1110–2820 K. The measured data were compared with predictions based on the Landau–Teller model and the StS approach to illustrate the differences between experiments and model predictions and to improve the performance of the 2-T model. The methodologies of the shock tube, TDLAS system, Landau–Teller model, and StS approach are presented in Sec. II. The experimental measurements and numerical results are presented and analyzed in Sec. III. Section IV presents concluding remarks.

II. METHODS

A. Shock tube

All experiments were performed in a kinetics shock tube with a driver section of 3.3 m, a driven section of 6.4 m, and an inner diameter of 10.07 cm. Detailed information is provided in Refs. 30 and 62. Four piezoelectric pressure transducers (PCB 113B26) were installed over the last 1.0 m of the shock tube to determine the velocity of the incident shock. The extrapolation method was used to access the shock velocity at the endwall. The temperature ($T_{5,0}$) and pressure ($p_{5,0}$) behind reflected shock waves were calculated based on one-dimensional normal-shock equations and initial temperature and pressure in the driven section. Considering the mixtures used in this study (Table I) are highly diluted in Ar, the pre-excitation of CO in this study is negligible for the interpretation of measured rotational and vibrational temperatures behind reflected shocks. Therefore, the vibrational energy of CO was not considered for calculating $T_{5,0}$ and $p_{5,0}$. All the pressure transducers were coated with a thin layer of silicon components to shield them from heat transfer and gas ionization. The transducer installed at 20 mm from the endwall was used to measure the pressure time histories for TDLAS measurements. Two opposite windows (made by CaF₂, effective spectral range: 0.18–8.00 μm) were fixed at the same

cross section. The windows were wedged at 3° to avoid the unwanted beam interferences caused by back reflection. After each shock, we opened the endwall and cleaned the broken diaphragms. The leakage rate of the shock-tube system is around 2.3×10^{-3} Pa/min, which ensures that the experiments are immune to leaking gases from the air.

Table I shows the detailed mixture compositions and experimental conditions used in this study. All the mixtures were prepared based on the partial pressure method and allowed to rest for at least 12 h before use to ensure homogeneity. Mixture 1 was used for T_{rot} , T_{vib} , and vibrational relaxation time measurements. Mixtures 2 and 3 were used to assess the accelerating effects of He and H₂ on the vibrational relaxation of CO. To diminish the impact of adsorption gases on the relaxation process of CO, the test mixtures were used to wash and clean the driven section before each shock. To minimize the effect of gas motion, the mixture was fed into the driven section and rested for at least 5 min before running the shock.

H₂O was found to have a significant acceleration effect on the vibrational relaxation process of CO due to the near-resonance transfer between CO vibration and either H₂O rotation or the H₂O vibrational bending mode.¹³ The authors of the work of von Rosenberg *et al.*⁶³ summarized $p\tau(\text{CO-H}_2\text{O})$ as 0.17 atm· μs in 1230–2600 K. Therefore, the test gases were highly purified. The purities of CO, He, and H₂ reach 99.999% and the purity of Ar reaches 99.9999% with H₂O concentration lower than 400 ppb (Air Liquide).

B. TDLAS system

Figure 1 shows the schematic diagram of the TDLAS setup,³⁰ which is briefly described here. The system can be divided into the laser part, the detection part, and the wavelength-calibration part. In the laser part, three continuous-wavelength interband-cascade lasers (Nanoplus) were used to access the P(0, 21), P(1, 21), and P(0, 37) lines in the fundamental vibrational band of

TABLE I. Mixture compositions and experimental conditions.

Mixture No.	CO (mol. %)	He (mol. %)	H ₂ (mol. %)	Ar (mol. %)	p (bar)	T (K)
1	1.0	99.0	1.4–3.8	1590–2730
2	1.0	1.0	...	98.0	1.6–2.7	1150–2820
3	1.0	...	1.0	98.0	1.5–2.8	1110–2810

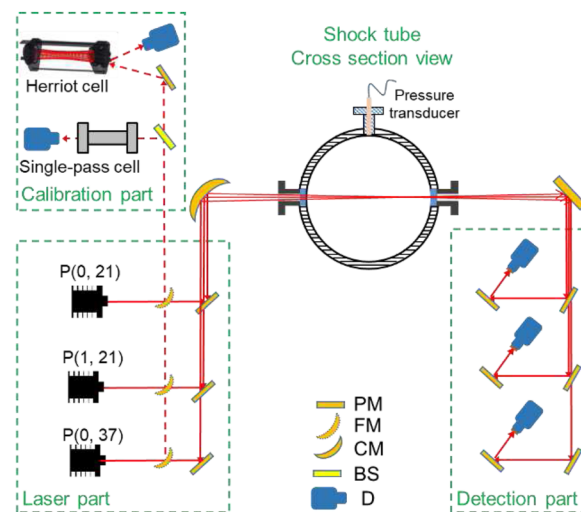


FIG. 1. Schematic of the TDLAS setup (PM, plane mirror; FM, flip mirror; CM, concave mirror; BS, beam splitter; D, detector).

CO. The three laser beams were focused into the shock tube by a concave mirror. In the detection part, three mid-infrared detectors (Vigo, PVI-4TE-5, bandwidth: 10 MHz) were used to detect the corresponding beam from the respective laser. Three bandpass filters (Hangzhou Multi IR Technology, INBP-4870–220 nm; Spectrogon, BP-4950–200 nm and NB-5040–155 nm) were fixed in front of the detectors to shield the thermal emission. The fixed-wavelength direct-absorption method was used in this study to ensure a measurement time resolution of 1 μ s. Thus, in the wavelength-calibration part, a single-pass cell (33.8 cm) and a long-path Herriot cell (25.56 m) were used to position the wavelength of the laser beams.

When a narrow-bandwidth laser beam transmits through a uniform gas medium, the attenuation of the incident laser beam intensity follows the Beer–Lambert law,

$$-\ln(I_t/I_0) = pS(T)x_iL\varphi(\nu_{ji}), \quad (1)$$

where I_t is the intensity of the transmitted laser beam, I_0 is the intensity of the incident laser beam, p (atm) is the pressure, $S(T)$ ($\text{cm}^{-2} \text{atm}^{-1}$) is the temperature-dependent line strength, x_i is the mole fraction of the target species, L (cm) is the optical

path, ν_{ji} (cm^{-1}) is the wavenumber of the spectral line transition in the vacuum, and $\varphi(\nu_{ji})$ (cm) is the line shape function (Voigt in this work). The temperature-dependent spectral line intensity $S_{ji}(T)$ of the rovibrational transition [$\text{cm}^{-1}/(\text{molecule cm}^{-2})$] can be expressed as

$$S_{ji}(T) = I_a \frac{A_{ji}}{8\pi c \nu_{ji}^2} \frac{g' \exp\left(-\frac{c_2 E''}{T}\right) \left[1 - \exp\left(-\frac{c_2 \nu_{ji}}{T}\right)\right]}{Q(T)}, \quad (2)$$

where I_a is the natural terrestrial isotopic abundance, A_{ji} (s^{-1}) is the Einstein coefficient for spontaneous emission, c (cm s^{-1}) is the light speed, g' is the upper state statistical weight, c_2 (cm K) is the second radiation constant, E'' (cm^{-1}) is the lower-state energy, and $Q(T)$ is the partition function. These parameters can be inferred directly from the most recent spectroscopic databases.^{64,65}

In thermal nonequilibrium states, assuming that the rotational and vibrational energy distributions of the target molecule independently follow the Boltzmann distributions with T_{rot} and T_{vib} , the T_{rot} - and T_{vib} -dependent line intensity of a rovibrational transition line can be expressed as

$$S_{ji}(T_{rot}, T_{vib}) = I_a \frac{A_{ji}}{8\pi c \nu_{ji}^2} \frac{g' \exp\left[-c_2 \left(\frac{E''_{rot}}{T_{rot}} + \frac{E''_{vib}}{T_{vib}}\right)\right] \left\{1 - \exp\left[-c_2 \left(\frac{\Delta E_{rot}}{T_{rot}} + \frac{\Delta E_{vib}}{T_{vib}}\right)\right]\right\}}{Q_{rot}(T_{rot})Q_{vib}(T_{vib})}, \quad (3)$$

where $Q_{rot}(T_{rot})$ is the rotational partition function, $Q_{vib}(T_{vib})$ is the vibrational partition function, E''_{rot} (cm^{-1}) is the rotational lower-state energy, E''_{vib} (cm^{-1}) is the vibrational lower-state energy, ΔE_{rot} (cm^{-1}) is the rotational transition energy change, and ΔE_{vib} (cm^{-1}) is the vibrational transition energy change. The authors of this study selected three transition lines in the fundamental vibrational band of CO, P(0, 21), P(1, 21), and P(0, 37), for time-dependent T_{rot} and T_{vib} measurement. Figure 2 shows that the line-strength ratio of the P(0, 21)/P(1, 21) line pair is strongly T_{vib} dependent while the line-strength ratio of the P(0, 21)/P(0, 37) line pair is strongly T_{rot} dependent. Therefore, the P(0, 21)/P(1, 21) line pair is used for T_{vib} measurement and the P(0, 21)/P(0, 37) line pair is used for T_{rot} measurement. The calibrated line strength and collisional broadening data are those provided in our previous study.³⁰ We checked that, in the target temperature range, there are no absorbance interferences of He and H₂ at the line center of the selected lines. In addition, our previous studies^{30,62} showed that the three lines were free from the absorbance interferences of H₂O and CO₂ in the ambient.

An iterative method was used to automatically calculate the time-dependent T_{rot} and T_{vib} values based on Eqs. (1) and (3). The measured I_0 , I_t , and pressure profiles were used as initial inputs. Detailed data processing for calculating T_{rot} and T_{vib} is referred to in Ref. 30.

C. Landau-Teller model and Millikan-White vibrational relaxation time

In the 2-T framework,³⁹ the differential equation in Eq. (4) developed by Landau and Teller⁴⁰ is used to describe the

vibrational energy transfer during the vibrational relaxation process of CO,

$$\frac{de_{vib}}{dt} = \frac{\bar{e}_{vib}(T_{tr}) - e_{vib}(T_{vib})}{\tau(T_{tr})}, \quad (4)$$

with e_{vib} being the vibrational energy, $\bar{e}_{vib}(T_{tr})$ the equilibrium value of the vibrational energy, and τ the vibrational relaxation time. The vibrational energy was calculated based on Eq. (5) assuming CO as a simple harmonic oscillator,

$$e_{vib} = \frac{\theta_{vib}/T_{vib}}{e^{\theta_{vib}/T_{vib}} - 1} RT_{vib}, \quad (5)$$

with θ_{vib} the characteristic temperature of the oscillator (3122 K for CO) and R the universal gas constant. Millikan and White¹⁸ proposed the following expression for calculating the vibrational relaxation data based on a large number of measured data:

$$\ln(p\tau) = -18.42 + A \left(T_{tr}^{-1/3} - 0.015\mu^{1/4} \right), \quad (6)$$

with μ being the reduced mass of the colliding pair and A the fitting parameter. In addition, the vibrational relaxation time of CO in a multicomponent mixture, $\tau_{CO,mix}$, was calculated based on the following equation:

$$\tau_{CO,mix}^{-1} = x_{CO}\tau_{CO-CO}^{-1} + \sum_i x_i \tau_{CO-i}^{-1}, \quad (7)$$

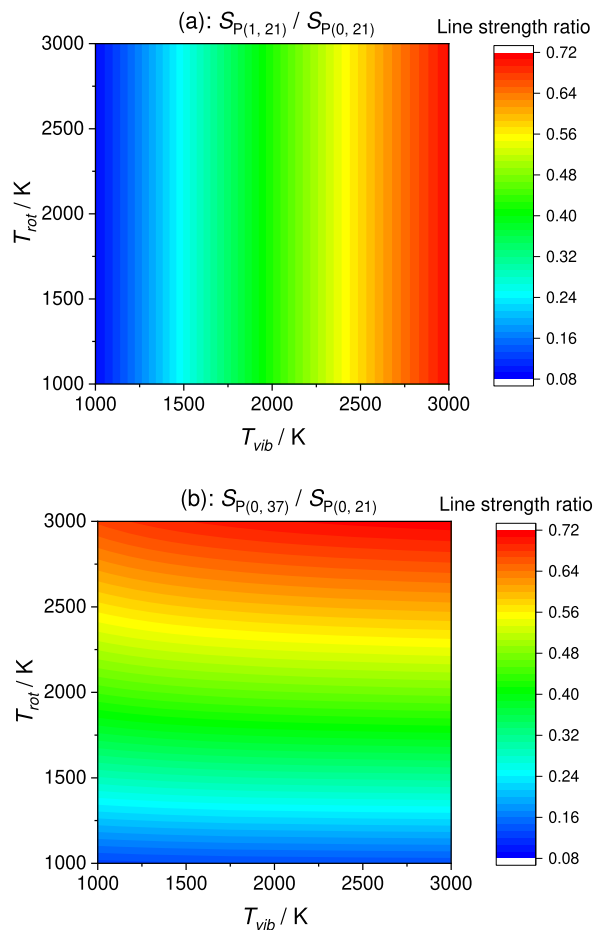


FIG. 2. Line-strength ratios as a function of T_{rot} and T_{vib} . (a) P(0, 21) and P(1, 21) line pair. (b) P(0, 21) and P(0, 37) line pair.

with x_{CO} being the mole fraction of CO, τ_{CO-CO} the vibrational relaxation time of collisions between CO and CO, x_i the mole fraction of the collider i , and τ_{CO-i} the vibrational relaxation time of collisions between CO and collider i . In short, the time-dependent T_{vib} was obtained from the theoretical model developed by Landau and Teller⁴⁰ [Eq. (4)] and vibrational relaxation time summarized by Millikan and White¹⁸ [Eq. (6)].

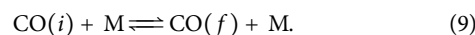
D. State-to-state calculation

The vibrational StS approach treats each vibrational energy state as a pseudo-species and represents the nonequilibrium vibrational distribution function of molecules. The translational-rotational equilibrium is assumed to happen much faster than the translational-vibrational one, which is a good approximation in the present cases, as validated by the experimental data of Sec. III A. A total of 20 lowest vibrational levels of CO ($\nu = 0-19$, whose vibrational energies are determined using the Morse parameters used in Ref. 50, i.e., $\omega_e = 2169.81 \text{ cm}^{-1}$, $x_e = 0.006125$, and $y_e = 0.0000048$) are considered in the present work. Although

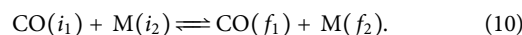
the number of considered vibrational states is less than the maximum vibrational number of CO at its ground electronic state, it is seen in Sec. III D that the number densities of the vibrational states with ν higher than 20 are significantly low and negligible under the conditions used in the present work. Moreover, under the circumstances of the present reflected shock conditions, the highest temperature is less than 3000 K and the molecule CO is highly diluted; so, the chemical reactions are not important and they can be neglected in the following StS calculations, which then only take the vibrational relaxation processes [i.e., vibration-translation (V-T) bound-bound transitions for CO-atom collisions and vibration-vibration-translation (V-V-T) bound-bound transitions for CO-molecule collisions] into account. Therefore, the master equations of the CO vibrational state i behind the reflected shock wave can be written as follows:

$$\begin{aligned} \frac{\partial[\text{CO}(i)]}{\partial t} = & \sum_{M=\text{atoms}} \sum_{f \neq i} \left\{ k_{V-T,CO-M}(f \rightarrow i)[\text{CO}(f)][M] \right. \\ & \left. - k_{V-T,CO-M}(i \rightarrow f)[\text{CO}(i)][M] \right\} \\ & + \sum_{M=\text{molecules}} \sum_{i_2} \sum_{f_1} \sum_{f_2} \left\{ k_{V-V-T,CO-M}(f_1, f_2 \rightarrow i, i_2) \right. \\ & \times [\text{CO}(f_1)][M(f_2)] - k_{V-V-T,CO-M}(i, i_2 \rightarrow f_1, f_2) \\ & \left. \times [\text{CO}(i)][M(i_2)] \right\}, \end{aligned} \quad (8)$$

in which square bracket $[\cdot]$ represents the number density of species and $k_{V-T,CO-M}$ is the rate coefficient of the following V-T bound-bound transitions for CO-M collisions (herein M denotes atom, in this paper M = Ar or He):



Moreover, $k_{V-V-T,CO-M}$ is the rate coefficient of the following V-V-T bound-bound transitions for CO-M collisions (herein M denotes diatom, in this paper M = CO or H₂):



The key step in performing the StS calculation is to obtain the accurate values of the above state-to-state rate coefficients. In this study, the mixed Quantum-Classical (MQC) method, introduced by Billing⁶⁶ in the version developed by the authors,^{67,68} is used to calculate the processes represented by Eq. (9). The MQC method recovers quantum effects associated with the vibrational motion,⁶⁶⁻⁶⁸ which are the most relevant ones in the V-T and V-V-T processes, yet for the remaining degrees of freedom a classical dynamics description is kept. The V-T rate coefficient dataset of CO-He collisions (covering $\nu = 0-10$ of CO vibrational states) was calculated by the MQC method based on the *ab initio* potential energy surface (with improved long-range behavior) of McBane.⁶⁹ Specifically, 47 initial values of total classical (translation + rotation) energy comprised between 50 and 80 000 cm^{-1} , with a more frequent sampling directed toward lower energies, were considered in the MQC calculations. Two thousand trajectories were used for each energy value with an initial separation distance atom-diatom R at 15 Å and a maximum value of the impact parameter of 9 Å was

used. The coupled time-dependent quantum equations were solved for the vibrational motion comprising vibrational states ν satisfying $\Delta\nu = \pm 9$. Figure 3(a) reports the rate coefficients for the V–T process $\text{CO}(\nu_i = 1) + \text{He} \rightarrow \text{CO}(\nu_f = 0) + \text{He}$ for $T = 300\text{--}6000$ K, and it is seen that the calculated MQC results strongly increase with temperature and are in good agreement with the available experimental values.^{14,70} The V–T rate coefficients (for a fixed $\Delta\nu$ process) also increase with the ν_i quantum number due to decrease in the energy deficit, as seen in the StS rate coefficient datasets in the supplementary material, S1. The results obtained by the forced harmonic oscillator (FHO) model⁴⁸ are also shown in Fig. 3(a). Details of the FHO model can be found in Ref. 71. Specifically, in order to achieve the best fit of the FHO results to the available experimental rate coefficients for the CO–He collision, a Morse intermolecular potential $V(R) = E_m \cdot [1 - \exp(-\alpha R)]^2$ was adopted with $E_m = 30$ K,⁶⁹ $\alpha = 3.5 \text{ \AA}^{-1}$, and the steric factor for V–T process S_{V-T} equals $4/9$ as proposed in the work of Adamovich *et al.*⁴⁸ and the collisional cross section σ equals 35 \AA^2 . It is seen in Fig. 3(a) that the FHO rate coefficients are close to the MQC data and experimental values at a temperature range of $1000\text{--}3000$ K (within the conditions reported in Table I). Moreover, for the CO–Ar collision, the V–T rate coefficients were calculated by the MQC method based on the three-dimensional potential energy surface of Sumiyoshi and Endo^{72,73} (in the version developed in Ref. 73). The same computational settings of the MQC calculations of the above CO–He system were adopted for the CO–Ar collision. Figure 3(b) shows the V–T rate coefficients of the process $\text{CO}(\nu_i = 1) + \text{Ar} \rightarrow \text{CO}(\nu_f = 0) + \text{Ar}$, and it is seen that the calculated MQC results are in good agreement with the fitting experimental data of Ref. 74 when the temperature is larger than 2000 K, while slight deviation is found at lower temperatures. However, it is noted that the available potential energy surface of Sumiyoshi and Endo^{72,73} describes the CO bond length only from 1.0 to 1.35 \AA , so the V–T rate coefficients calculated based on this PES are only accurate for ν up to 4 . Therefore, the FHO model⁴⁸ was used instead to obtain the V–T rate coefficient dataset of the CO–Ar

collision, covering $\nu = 0\text{--}19$ of CO vibrational states. Specifically, for the present FHO calculations of the CO–Ar collision, a Morse intermolecular potential $V(R) = E_m \cdot [1 - \exp(-\alpha R)]^2$ was adopted with $E_m = 200$ K, $\alpha = 4.15 \text{ \AA}^{-1}$, $S_{V-T} = 4/9$, and $\sigma = 44 \text{ \AA}^2$. It is demonstrated in Fig. 3(b) that the FHO (using the above parameters) rate coefficients of the process $\text{CO}(\nu_i = 1) + \text{Ar} \rightarrow \text{CO}(\nu_f = 0) + \text{Ar}$ agree perfectly with the fitting experimental data of Ref. 74, and the FHO results overlap with the MQC data above 3000 K and become slightly lower below this threshold. A comparative analysis of the results in Figs. 3(a) and 3(b) unequivocally shows that the CO–He collision is more effective than the CO–Ar collision at the same temperature, and the efficiency of the former collision partner is attributed to the lower reduced mass thanks to the significantly lower mass of helium.

For the CO–diatom collisions, i.e., CO–CO and CO–H₂ collisions considered in this study, the number of V–V–T bound–bound transitions of Eq. (10) are massive, so it is very time-consuming to use the MQC method to generate the database. Therefore, we adopted the semiclassical FHO model to obtain the V–V–T rate coefficients of CO–diatom collisions. Specifically, for the CO–CO collision, a Morse intermolecular potential $V(R) = E_m \cdot [1 - \exp(-\alpha R)]^2$ was adopted with $\alpha = 4.5 \text{ \AA}^{-1}$ and $E_m = 180$ K, which is close to the potential well in the parallel configuration (with two CO monomers at their equilibrium bond distances) of the highly accurate six-dimensional potential energy surface of the CO + CO system developed in Ref. 75. The steric factor for the V–T process S_{V-T} equals $4/9$ and for the V–V–T process S_{V-V-T} equals $1/27$, as proposed in the work of Adamovich *et al.*,⁴⁸ and the collisional cross section σ equals 44.5 \AA^2 . It is seen in Fig. 4(a) that the FHO (using the above parameters) rate coefficients of the process $\text{CO}(\nu_i = 1) + \text{CO}(w_i = 0) \rightarrow \text{CO}(\nu_f = 0) + \text{CO}(w_f = 0)$ agree well with the available experimental values.^{18,76} The FHO model with the above settings was then used to calculate the V–V–T rate coefficients of the CO–CO collision, covering $\nu_i = 0\text{--}19$ and $w_i = 0\text{--}19$ of two CO monomers. Moreover, for

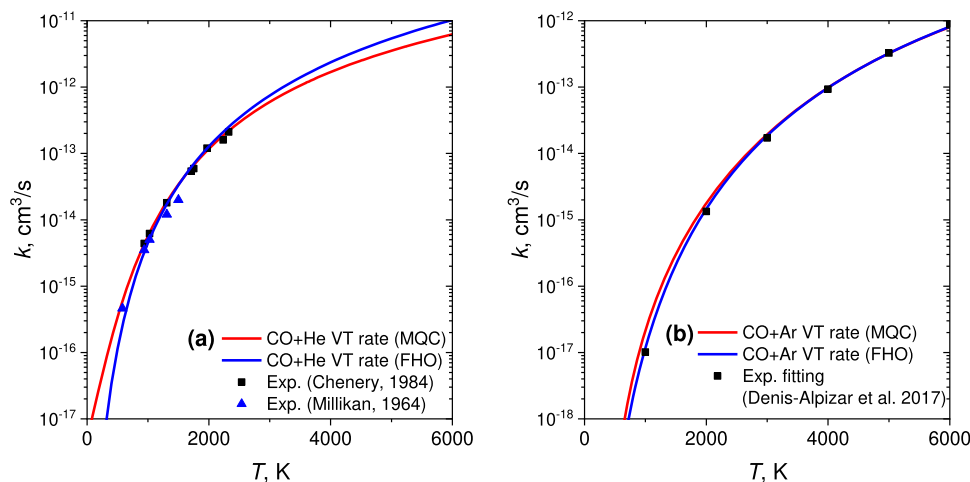


FIG. 3. (a) Rate coefficients for the V–T process $\text{CO}(\nu_i = 1) + \text{He} \rightarrow \text{CO}(\nu_f = 0) + \text{He}$ calculated by the MQC method, and experimental data of Refs. 14 and 70 are also reported. (b) Rate coefficients for the V–T process $\text{CO}(\nu_i = 1) + \text{Ar} \rightarrow \text{CO}(\nu_f = 0) + \text{Ar}$ calculated by the MQC method and FHO model, and the fitting experimental data of Ref. 74 are also shown.

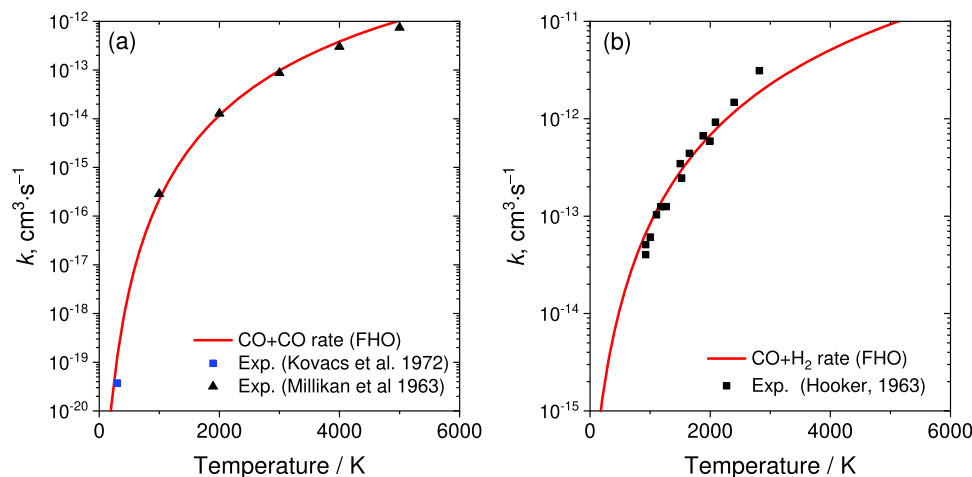


FIG. 4. (a) Rate coefficients for the process $\text{CO}(v_i = 1) + \text{CO}(w_i = 0) \rightarrow \text{CO}(v_f = 0) + \text{CO}(w_f = 0)$ calculated by the FHO model, and experimental data of Refs. 18 and 76 are also reported. (b) Rate coefficients for the process $\text{CO}(v_i = 1) + \text{H}_2(w_i = 0) \rightarrow \text{CO}(v_f = 0) + \text{H}_2(w_f = 0)$ calculated by the FHO model, and the experimental data of Ref. 12 are also shown.

the CO–H₂ collision, the FHO parameters are set as follows: $E_m = 200$ K (chosen in the same order of magnitude as the above CO–CO collision), $\alpha = 5.1 \text{ \AA}^{-1}$ (tuned to obtain good agreement with the experimental rate coefficients reported in the following), $S_{V-T} = 4/9$, $S_{V-V-T} = 1/27$, and $\sigma = 40.0 \text{ \AA}^2$. Figure 4(b) shows that the FHO rate coefficients of the process $\text{CO}(v_i = 1) + \text{H}_2(w_i = 0) \rightarrow \text{CO}(v_f = 0) + \text{H}_2(w_f = 0)$ agree well with the available experimental values¹² at a temperature range of 1000–3000 K, within the interested reflected shock wave conditions in the present study. It is clearly shown by comparing the data in Figs. 4(a) and 4(b) that the CO–H₂ collision is significantly more effective than the CO–CO collision due to mass effects. The FHO model with the above parameters was then used to calculate the V–V–T rate coefficients of the CO–H₂ collision, covering $v_i = 0\text{--}19$ of CO and $w_i = 0\text{--}1$ of H₂ (The energies are taken from Ref. 77. Note that $\omega_e = 4401.2 \text{ cm}^{-1}$ for H₂⁶⁹ is much higher than $\omega_e = 2169.8 \text{ cm}^{-1}$ for CO. As a result, the energy spacing in H₂ is much greater, and adding more vibrational states of H₂ does not yield any discernible differences in the present results due to their much lower population). All the above state-to-state rate coefficient datasets of Eqs. (9) and (10) are available in the supplementary material, S1.

The master equations of CO vibrational states, Eq. (8), were solved by the variable-order variable-step implicit method.⁷⁸ The initial number densities of CO vibrational states are evaluated by Boltzmann distribution under the experimentally measured vibrational temperature immediately behind the reflected shock wave. Previous studies^{8,9,37,38} have shown that the temperature and pressure instabilities induced by the nonideal effects of shock tube significantly affect the thermodynamic states and reactivities of the reactive mixtures. Using measured pressure and temperature profiles as inputs during kinetics simulation helps diminish the influences caused by the gaps between experiments and simulations. Therefore, the measured pressure and temperature profiles were applied to the predictions based on the Landau–Teller model and the predictions of the StS approach. In each time

step, the vibrational energy was allowed to transfer at a constant-volume state and then the mixture was isentropically compressed (or expanded).

The StS calculation gives detailed information on the population of vibrational energy states (vibrational distribution function), from which one can extract the values of macroscopic vibrational temperatures, i.e., the vibrational temperature of the first-excited state $T_{v,1}$ and the average vibrational temperature T_v (whose definition will be given in Sec. III D). Specifically, $T_{v,1}$ is defined in a general form as the number density ratio of the first-excited state to the ground state, i.e.,

$$T_{v,1} = \frac{e_v(1) - e_v(0)}{k_B \ln([\text{CO}(1)]/[\text{CO}(0)])}, \quad (11)$$

where $e_v(i)$ is the vibrational energy of vibrational state i . Since the experimental data of T_v obtained in this work is measured from the $P(0, 21)/P(1, 21)$ line pair, it can be characterized by Eq. (11).

III. RESULTS AND DISCUSSION

A. Rotational and vibrational temperature time histories of mixtures 1–3 behind reflected shock waves

In this section, the time-dependent T_{rot} and T_{vib} measurements are shown during the vibrational relaxation processes of CO in mixtures 1–3 behind reflected shock waves. Detailed information (including the fill gas pressure and temperature in the low-pressure driven section, the velocity of the incident and reflected shocks, the velocity of the gas behind the incident shocks, and the raw data of measured pressure, rotational temperature, and vibrational temperature) of all the experiments is provided in the supplementary material, S2. The measured data were compared with predictions based on the Landau–Teller model and the StS approach to reveal the physicochemical processes of thermal

nonequilibrium CO. Specifically, for the measured data, the Landau–Teller model predictions, and StS simulations, the vibrational relaxation time is evaluated based on the time point when the vibrational energy of CO reaches $(1 - e^{-1})$ its equilibrium value. We checked that for the Landau–Teller predictions, the obtained vibrational relaxation time is almost equal to the data obtained based on the Millikan–White relationship.

Figure 5 shows the comparisons of different temperatures for shock-heated thermal nonequilibrium CO/Ar mixture (mixture 1) at $T_{5,0} = 1727$ K and $p_{5,0} = 3.8$ bar. The calculated temperature (black line) was obtained from $T_{5,0}$, $p_{5,0}$, measured pressure, and isentropic relationship, while T_{rot} (pink line) was measured by the P(0, 21)/P(0, 37) line pair. The abovementioned temperatures instantaneously reached a thermal equilibrium state after passage of the reflected shock and were highly consistent in the 1.2-ms time scale, indicating that the translational and rotational degrees of freedom of CO quickly relaxed into equilibrium. The two temperatures do not show a decreasing trend because the CO in mixture 1 is highly diluted in Ar, and the vibrational energy of CO occupies only a small part of the internal energy of mixture 1. In addition, the two temperatures increased by ~ 50 K at 1.2 ms due to the unstable behaviors of temperature and pressure induced by nonideal effects inside the shock tube. On the contrary, the measured T_{vib} from the P(0, 21)/P(1, 21) line pair experienced a relaxation process and then reached a vibrational equilibrium state. The measured T_{vib} value was compared with predictions based on the Landau–Teller model

and the StS approach assuming the gas is in a constant-volume hot environment (heat bath), as shown in Figs. 5(a) and 5(b). In the simulations, the T_{vib} value was calculated starting from 522 K, considering it has been pre-excited by the incident shock in a time scale of ~ 60 μ s. The predictions based on the Landau–Teller model were obviously slower than the measured data and were lower than the experimental values in the equilibrium state. It is seen in Fig. 5(b) that, in the vibrational relaxation process, the predictions based on the StS approach agreed well with the measured data, but the predictions in the equilibrium state were slightly lower than the measured data. Furthermore, the measured pressure and temperature profiles were used as inputs for the calculations based on the Landau–Teller model and the StS approach, as shown in Figs. 5(c) and 5(d), respectively. The predictions from the Landau–Teller model were still slower than the measured data. However, the two were highly consistent in the equilibrium state. The predictions based on the StS approach agreed well with the measured data in both the excitation and equilibrium states. The use of measured pressure and temperature profiles as inputs helps reveal the effects of unstable gas-dynamic behaviors on the vibrational relaxation process of CO. Therefore, in the following part, the measured pressure and temperature profiles were used as inputs for the data processing of mixtures 2 and 3.

For specific experiments (for example, in Figs. 5–7 and Figs. 9–12), the measured vibrational temperature drops between the incident and reflected shock waves. This phenomenon is due to the

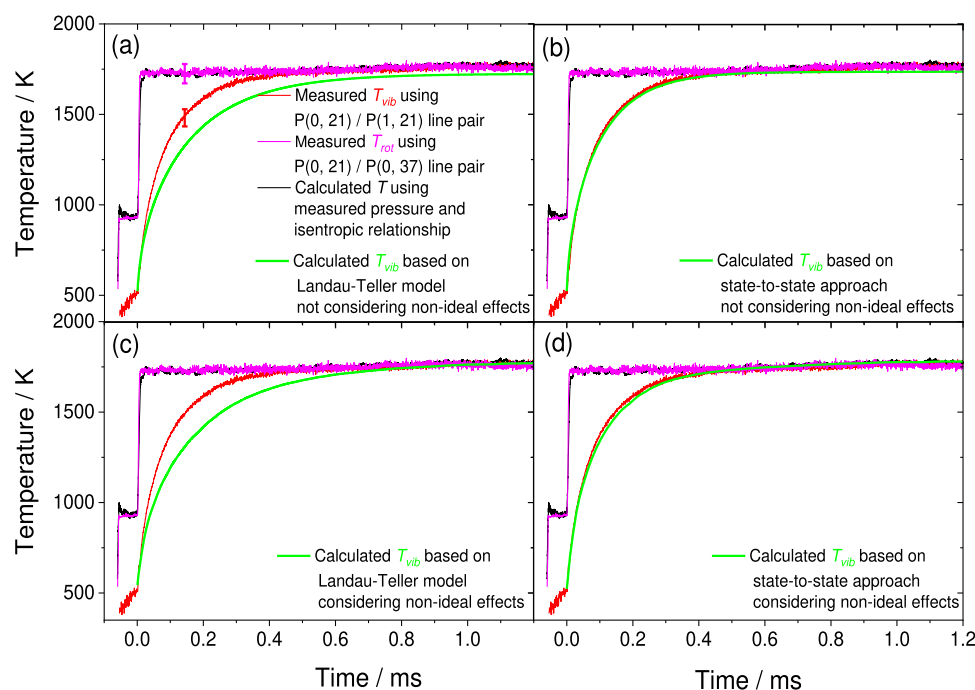


FIG. 5. Comparisons of different temperatures for shock-heated thermal nonequilibrium 1.0% CO/99.0% Ar mixture (mixture 1) at $T_{5,0} = 1727$ K and $p_{5,0} = 3.8$ bar. (a): The value of T_{vib} was calculated using the Landau–Teller model and the nonideal effects were not considered. (b): The value of T_{vib} was calculated using the StS approach and the nonideal effects were not considered. (c): The value of T_{vib} was calculated using the Landau–Teller model and the nonideal effects were considered. (d): The value of T_{vib} was calculated using the StS approach and the nonideal effects were considered.

beam schlieren effects caused by the incident and reflected shocks. The temperature of the unperturbed gas is at room temperature and beyond the trustable measurement temperature range of the current TDLAS. Therefore, in Figs. 5–7 and Figs. 9–12, the data before the arrival of the incident shock were removed.

The uncertainty in measured T_{vib} is 3.2% and in measured T_{rot} is 3.1%. For a detailed uncertainty analysis, the readers are referred to the work of He *et al.*^{30,62} The error bars are shown in the measured data on panel (a) of Figs. 5–7 and 12.

Figure 6 compares different temperatures during the vibrational relaxation process of the CO/Ar mixture with 1.0% He addition at $T_{5,0} = 1745$ K and $p_{5,0} = 2.2$ bar. Helium is a candidate to accelerate the vibrational relaxation process of CO during the calibration of high-temperature spectral data. In addition, helium is one of the choices for regulating the vibrational relaxation process of high-temperature thermochemical nonequilibrium gases.^{8,9} The addition of 1.0% He accelerated the relaxation process of CO. For mixture 2 in Fig. 6, the predictions based on the Landau–Teller model were still slower than the measured data while the results

calculated from the StS approach agreed well with the measured data. A detailed explanation for this phenomenon will be presented in Sec. III B.

Furthermore, the effects of 1.0% H₂ addition on the vibrational relaxation process of the CO/Ar mixture (mixture 3) at $T_{5,0} = 1578$ K and $p_{5,0} = 2.3$ bar are shown in Fig. 7. H₂ is a key intermediate during the combustion process of hydrocarbon fuels. In addition, H₂ is a commonly used molecule to accelerate the vibrational relaxation process of target species in the TDLAS measurements. Comparisons of different temperatures were similar to the aforementioned results shown in Figs. 5 and 6, and the StS results agreed well with the measured data. The effects of H₂ addition and the modifications on the Millikan–White vibrational relaxation data of the CO–H₂ system will be discussed in Sec. III B.

B. Vibrational relaxation data of mixtures 1–3

Figure 8 summarizes the vibrational relaxation data of mixtures 1–3 in the temperature range of 1110–2820 K. The vibrational relaxation data ($\rho \times \tau$) instead of the relaxation times were plotted

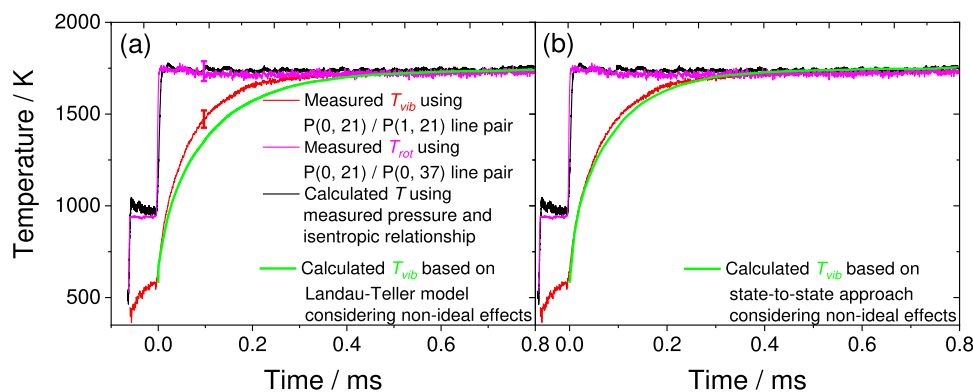


FIG. 6. Comparisons of different temperatures for shock-heated thermal nonequilibrium 1.0% CO/1.0% He/98.0% Ar mixture (mixture 2) at $T_{5,0} = 1745$ K and $p_{5,0} = 2.2$ bar. (a): The value of T_{vib} was calculated using the Landau–Teller model and the nonideal effects were considered. (b): The value of T_{vib} was calculated using the StS approach and the nonideal effects were considered.

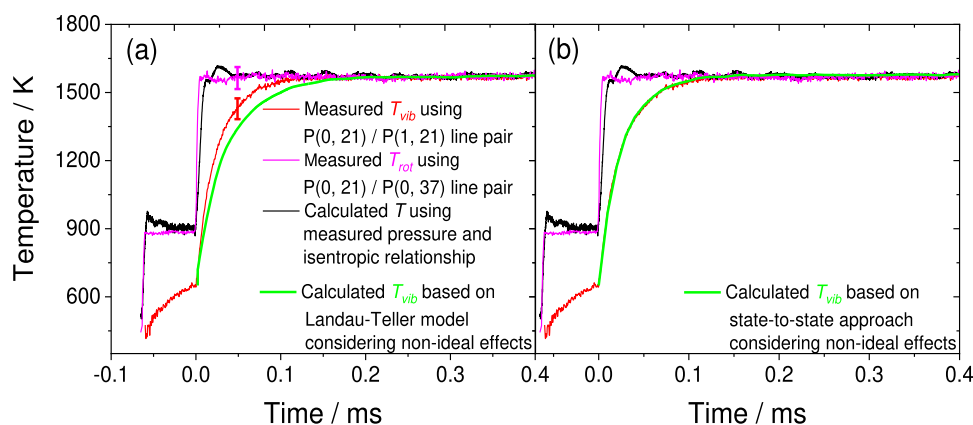


FIG. 7. Comparisons of different temperatures for shock-heated thermal nonequilibrium 1.0% CO/1.0% H₂/98.0% Ar mixture (mixture 3) at $T_{5,0} = 1578$ K and $p_{5,0} = 2.3$ bar. (a): The value of T_{vib} was calculated using the Landau–Teller model and the nonideal effects were considered. (b): The value of T_{vib} was calculated using the StS approach and the nonideal effects were considered.

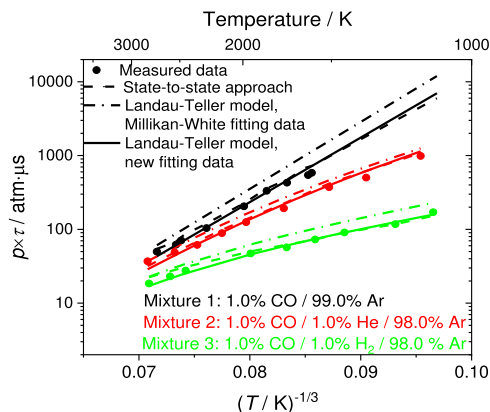


FIG. 8. Comparisons of vibrational relaxation data of mixtures 1–3 in the temperature range of 1110–2820 K.

TABLE II. Modifications for the Millikan–White relaxation data.

System	Original data, A	Corrected data, A
CO–Ar	213.00	202.55
CO–He	99.00	...
CO–H ₂	68.00	64.19

considering the latter are pressure-dependent. Adding 1.0% He and H₂ accelerated the vibrational relaxation process of CO, especially for H₂. The vibrational relaxation data exhibit approximately a linear relationship with $T^{-1/3}$ in the target temperature. Predictions based on the Landau–Teller model and StS approach were shown as comparisons. In the current temperature range, the predictions from the StS approach agreed well with the measured data for mixtures 1–3; however, the values predicted from the Landau–Teller model and Millikan–White fitting data¹⁸ were higher than the measured data, especially for mixtures 1 and 3. Based on the measured data

and the calculated data from the StS approach (extend to the low-temperature range where there is no measurement for the CO–Ar system), the fitting parameter, A , in the Millikan–White relationship was modified for the CO–Ar and CO–H₂ systems, as shown in Table II. The predictions based on the Landau–Teller model and the modified Millikan–White relaxation data agreed well with the measured data, as shown by the solid lines in Fig. 8.

The uncertainty in vibrational relaxation data is derived from each item in Eq. (7) using the Taylor series method of uncertainty propagation.⁷⁹ The uncertainty in concentrations of CO, He, and H₂ is 1.0%, while the uncertainty in Ar concentration is negligible. The uncertainty in $p \times \tau_{\text{CO-CO}}$ and $p \times \tau_{\text{CO-i}}$ is calculated based on the Millikan–White relaxation data, as shown in Eq. (6). The temperature used in Eq. (6) is derived from the shock wave velocity and 1D shock wave equation. Therefore, the uncertainty in T_{tr} is assumed as 1.0%. At 2000 K, the uncertainties in vibrational relaxation data for the three mixtures are all around 5.4%.

The value of T_{vib} of mixtures 1 and 2 was recalculated based on the Landau–Teller model and modified vibrational relaxation data of the CO–Ar system, as shown in Figs. 9(a) and 9(b), respectively. Compared with the results in Fig. 5(c) and 6(a), the calculated T_{vib} values agreed well with the measured data, indicating the reliability of the modified fitting parameter (A) for the CO–Ar system. Considering the good agreement between measured and calculated data for mixture 2, the fitting parameter for the CO–He system was not modified in the present study.

The value of T_{vib} for mixture 3 was recalculated based on the Landau–Teller model and modified vibrational relaxation data of the CO–Ar system and the CO–H₂ system, as shown in Fig. 10. As seen in Fig. 10(a), compared with the results in Fig. 7(a), the calculated data with modified relaxation data of the CO–Ar system were closer to the measured data, but there was still a gap. Furthermore, by also considering the modified data of the CO–H₂ system (in Table II), the predictions were highly consistent with the measured data, as shown in Fig. 10(b).

It is seen from the above results of mixture 2 that adding a small amount of helium accelerates the vibrational relaxation process of CO. The potential well depths of CO–Ar and CO–He

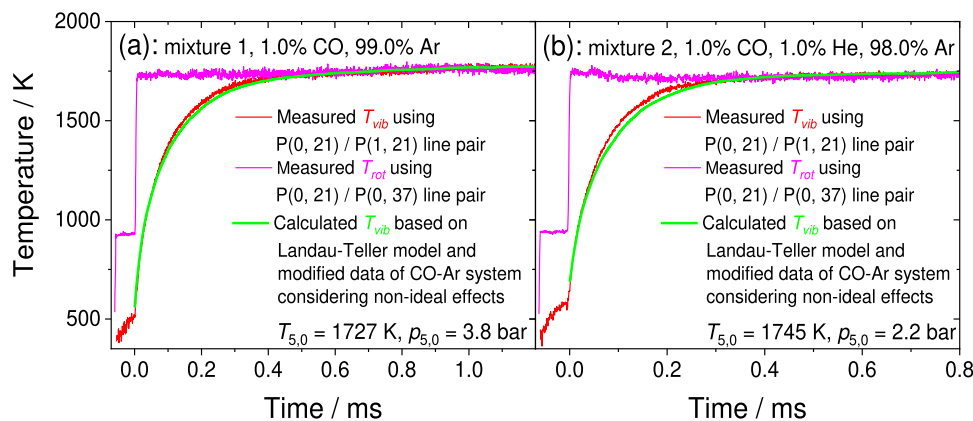


FIG. 9. Calculated T_{vib} based on the Landau–Teller model and modified vibrational relaxation data for (a): mixture 1 and (b): mixture 2.

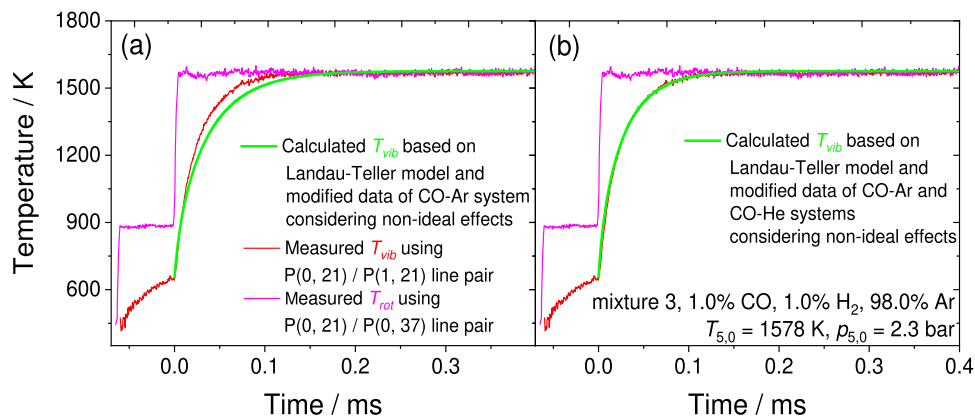


FIG. 10. Calculated T_{vib} based on the Landau–Teller model and modified vibrational relaxation data for mixture 3. (a): The modified data of the CO–Ar system was considered. (b): The modified data of CO–Ar and CO–He systems were considered.

systems are 107.1 cm^{-172} and 22.34 cm^{-1} ,⁶⁹ which show weakly bound of both systems and are not significantly different. Given this, the main reason for helium acceleration is that CO–He collisions are more effective than CO–Ar (and CO–CO) collisions due to the lower mass of helium. Vibrational relaxation is a velocity-dependent process,¹² so the reduced mass of the collision partners controls the magnitude of parameter A in Table II.

More appreciable acceleration occurs when adding a small amount of H_2 in mixture 3. The reason for this is either that the near-resonance process [V–R process, i.e., $\text{CO} (v = 1) + \text{H}_2 (j) \rightarrow \text{CO} (v' = 0) + \text{H}_2 (j')$] comes into play or the low reduced mass of CO– H_2 collision. However, the former case is almost independent of the temperature and is anticipated to be less efficient than the V–T process⁸⁰ (which increases fast with temperature) at

the temperatures of the present conditions. Therefore, the lowest reduced mass results in the lowest parameter A of CO– H_2 collision in Table II.

The optical windows for the TDLAS system were fixed at 20 mm from the endwall of the driven section. In each experiment, the gas mixture near the endwall region was first compressed and heated by the incident shock wave. Then, the reflected shock wave will compress and heat the gas mixture again. Herein, mixture 3 was used as an example to show the comparisons of different temperatures and to reveal the real states behind the incident shock, as shown in Fig. 11. The measured T_{rot} (pink line) instantaneously reached an equilibrium state after passage of the incident shock. CO was pre-excited by the incident shock and the measured T_{vib} of CO (red line) increased over time. The predictions based on the

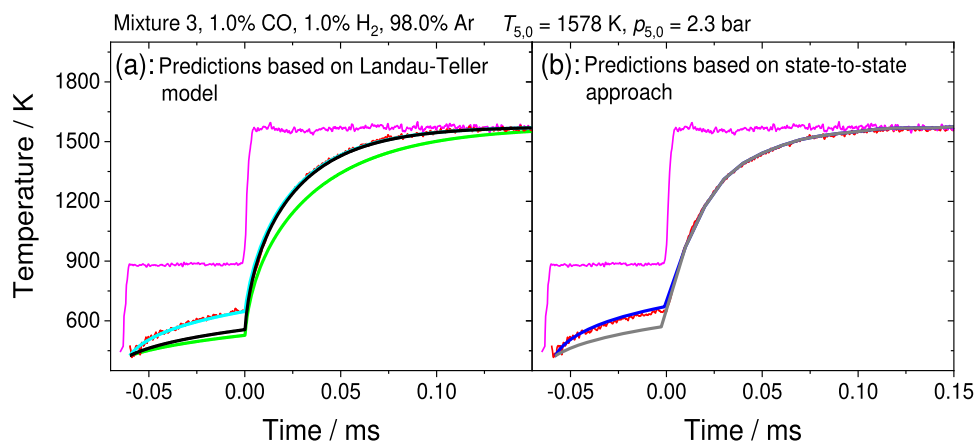


FIG. 11. Comparisons of different temperatures behind the incident and reflected shock waves. Pink line, measured T_{rot} ; red line, measured T_{vib} ; green line, calculated T_{vib} based on the Landau–Teller model and original Millikan–White fitting data; black line, calculated T_{vib} based on the Landau–Teller model and updated vibrational relaxation data; cyan, calculated T_{vib} based on the Landau–Teller model, updated vibrational relaxation data, and corrected time coordinates; gray line, calculated T_{vib} based on the StS approach; blue line, calculated T_{vib} based on the StS approach and corrected time coordinate. (a): The T_{vib} value was calculated using the Landau–Teller model. (b): The value of T_{vib} was calculated using the StS approach.

Landau–Teller model are shown in Fig. 11(a). The green line represents the calculated T_{vib} based on the original Millikan–White fitting data.¹⁸ It is expected that the calculated T_{vib} is slower than the measured data. The black line represents the calculated T_{vib} based on the modified Millikan–White relaxation data. The calculated data showed good agreement with the measurements behind the reflected shock but were still slower than the measured values in the region behind the incident shock. Hooker and Millikan¹² pointed out that the vibrational relaxation time is in the laboratory coordinates for the conditions behind the incident shock. It must be converted into the gas time coordinates by multiplying by the density ratio across the shock, considering there is gas velocity behind the incident shock and the observer's time scale differs from the internal one. Therefore, the vibrational relaxation data were modified with the density ratio and the calculated T_{vib} (cyan line) agreed well with the measured data. The corresponding predictions based on the StS approach are shown in Fig. 11(b). Considering the theoretical stagnation state behind reflected shocks, we assumed that the observer's time scale is equal to the internal time scale behind reflected shocks and the coordinate conversion was not considered for the vibrational temperature calculations in Figs. 5–7, 9, and 10. It should be noted that the time coordinate transformation must be considered for the vibrational relaxation studies in the complex flow field.

C. Effects of H₂O

Previous studies^{13,63} have highlighted that the near-resonance transfer between CO vibration and H₂O rotation or the H₂O vibrational bending mode efficiently accelerates the vibrational relaxation process of CO. The air contains H₂O. The test gas can be easily contaminated by moist air through shock tubes, the gas mixing vessel, and/or connection parts. Additionally, H₂O is easily enriched in gas cylinders. Figure 12 shows the measured T_{vib} of mixture 1 from two experiments in our laboratory. The predictions based on the Landau–Teller model and modified vibrational relaxation data are also shown as a comparison. For the results in Fig. 12(a), the Ar was not specially purified and the measured data increased faster than the calculated data. For the results in Fig. 12(b), highly purified Ar (99.9999%) was used and the

shock-tube system was carefully checked to minimize the potential leakage; the measured data agreed well with the predicted values. Diminishing the interferences of H₂O is a key prerequisite for ensuring accurate T_{vib} time-history measurements, especially for mixture 1. Our future studies will especially focus on the acceleration effects of H₂O on the vibrational relaxation process of CO and try to obtain the near-resonance rate coefficient of vibrational energy transfer between CO and H₂O over a wide temperature range.

D. Characterization of the vibrational temperature

In addition to the vibrational temperature of the first-excited state $T_{v,1}$ defined in Eq. (11), one can also extract the average vibrational temperature T_v from StS results. Specifically, the average vibrational temperature is represented by the total vibrational energy as

$$\frac{\sum_i [\text{CO}(i)] e_v(i)}{\sum_i [\text{CO}(i)]} = \frac{\sum_i e_v(i) \exp(-e_v(i)/k_B T_v)}{\sum_i \exp(-e_v(i)/k_B T_v)}. \quad (12)$$

However, it is seen from Fig. 13 that the vibrational temperatures defined in the above two ways are very close in the present cases for mixtures 1–3 (the details of the cases are described in the caption). One reason is that the translational temperatures behind the reflected shock waves are less than 3000 K, so the CO molecules mostly populate in the ground and first-excited vibrational states, which comprise a large proportion of vibrational energy. Another cause for similar vibrational temperatures is that, as will be seen in Fig. 14, the lower vibrational states are easier to get to equilibrium than the higher states, and although the latter show a deviation from the Boltzmann population, their number densities are orders of magnitude lower than the former.

Figure 14 reports the nonequilibrium vibrational distribution functions of CO behind reflected shock waves for the above cases of mixtures 1–3. It is found that when $t = 0.05$ ms, the normalized population of higher vibrational levels of CO is significantly larger than the corresponding Boltzmann distribution and displays a state of “overpopulation,” because a large number of molecules

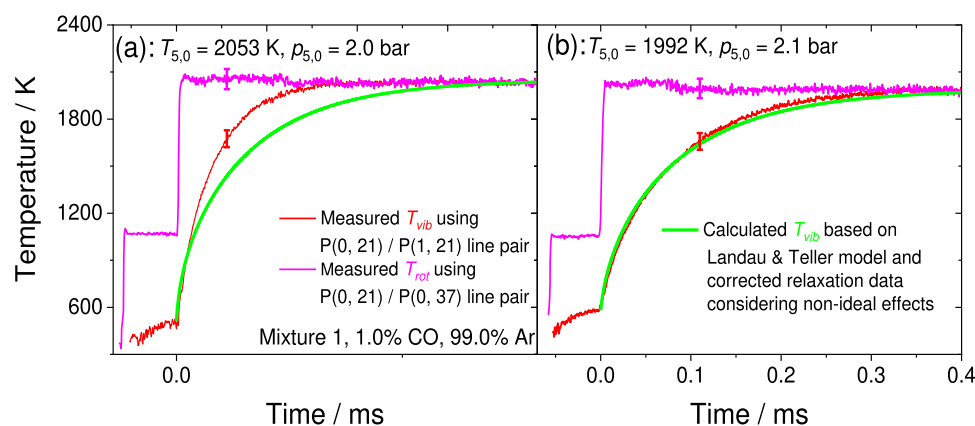


FIG. 12. Effects of H₂O on the vibrational relaxation process of CO. (a): $T_{5,0} = 2053$ K, $p_{5,0} = 2.0$ bar. (b): $T_{5,0} = 1992$ K, $p_{5,0} = 2.1$ bar.

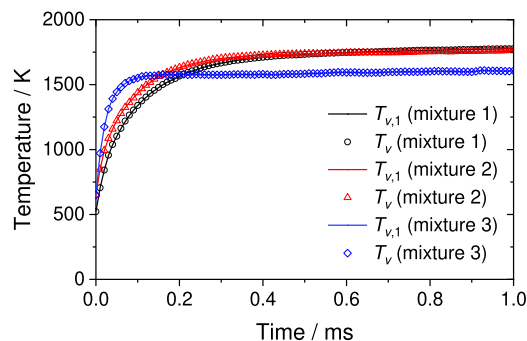


FIG. 13. Comparisons of the vibrational temperature of the first-excited state $T_{v,1}$ and the average vibrational temperature T_v for mixture 1: 1.0% CO/99.0% Ar mixture at $T_{5,0} = 1727$ K and $p_{5,0} = 3.8$ bar, mixture 2: 1.0% CO/1.0% He/98.0% Ar mixture at $T_{5,0} = 1745$ K and $p_{5,0} = 2.2$ bar, and mixture 3: 1.0% CO/1.0% H₂/98.0% Ar mixture at $T_{5,0} = 1578$ K and $p_{5,0} = 2.3$ bar.

from low vibrational levels are transitioned to high vibrational levels via the V–T energy transfer. Since the considered conditions depicted in Fig. 14 are in weak nonequilibrium, the vibrational distribution functions at $t = 0.05$ ms and $t = 0.10$ ms manifest as bi-modal Boltzmann distributions, which implies that one can trace two straight lines and reproduce well the nonequilibrium in these vibrational distributions. As time increases, the nonequilibrium population tends to Boltzmann population, and the system approaches equilibrium. It is obvious in Fig. 14(c) that the nonequilibrium population for the selected times because of the faster vibrational relaxation time of mixture 3 due to the existence of H₂. Moreover, it is found in Fig. 14 that, in the present cases of interest, the largest vibrational energy level ($i = 19$) considered herein is ten orders of magnitude less populated than the ground state, which shows why we chose an incomplete vibrational ladder of CO in this paper.

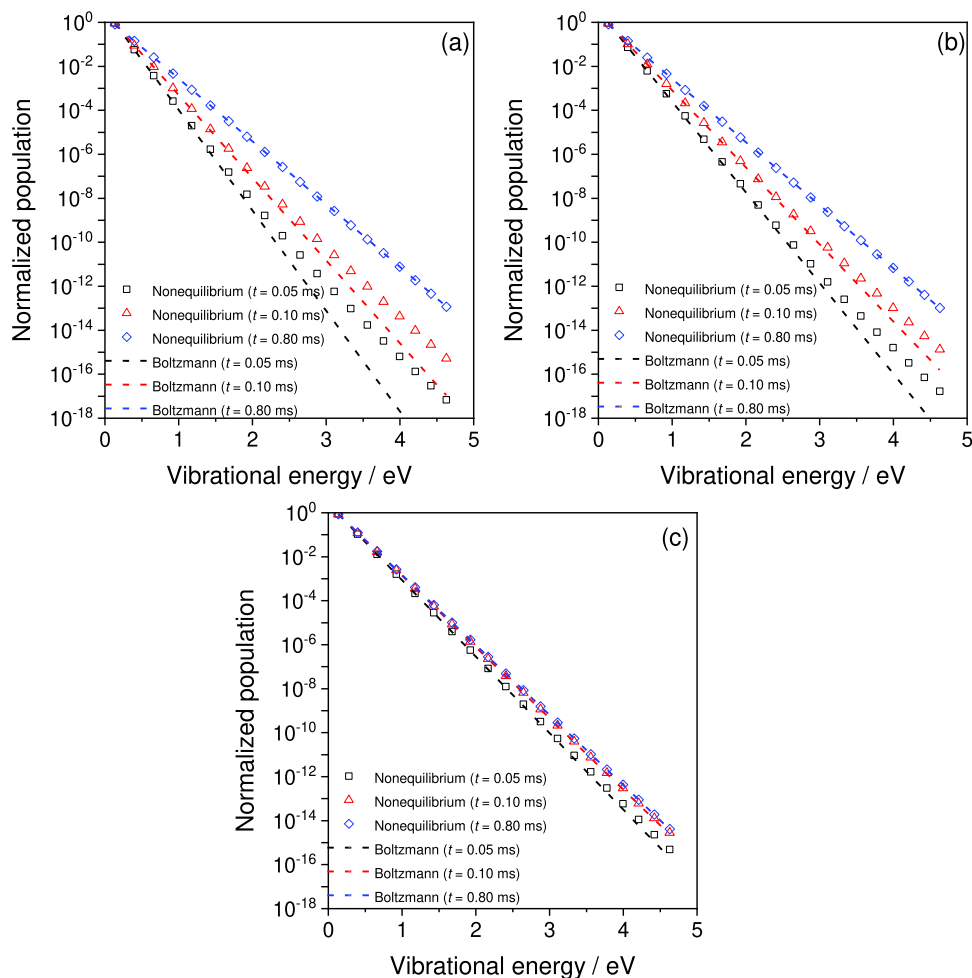


FIG. 14. Normalized population of vibrational energy levels of CO behind reflected shock waves for (a) mixture 1: 1.0% CO/99.0% Ar mixture at $T_{5,0} = 1727$ K and $p_{5,0} = 3.8$ bar, (b) mixture 2: 1.0% CO/1.0% He/98.0% Ar mixture at $T_{5,0} = 1745$ K and $p_{5,0} = 2.2$ bar, and (c) mixture 3: 1.0% CO/1.0% H₂/98.0% Ar mixture at $T_{5,0} = 1578$ K and $p_{5,0} = 2.3$ bar.

IV. CONCLUSION

In this study, three interference-free transition lines in the fundamental vibrational band of CO, P(0, 21), P(1, 21), and P(0, 37), were selected to develop the TDLAS system for simultaneous rotational and vibrational temperature time-history measurements during the vibrational relaxation process of CO with Ar, He, and H₂ as collision partners behind shock waves. The tunable mid-infrared lasers provided a fast, *in situ*, time-resolved, and state-specific method for rotational and vibrational temperature measurements by probing individual energy levels of the target species, and the TDLAS technique is well suited for the shock-tube studies on vibrational relaxation of CO.

As shown in the present experimental measurements, the rotational temperature instantaneously reached an equilibrium state after the passage of the shock wave and was found to agree well with the calculated temperature obtained from the measured pressure and isentropic relationship. The vibrational temperature experienced a vibrational relaxation process before reaching the equilibrium state. The time-dependent vibrational temperature and the summarized vibrational relaxation data ($p \times \tau$) were compared with predictions based on the Landau–Teller model and StS approach. The new datasets of the state-specific inelastic rate coefficients of CO–Ar, CO–He, CO–CO, and CO–H₂ collisions were calculated in this study using the mixed quantum-classical method and the semiclassical forced harmonic oscillator model. The StS approach showed very good performances in predicting the time-dependent vibrational temperature and vibrational relaxation data of CO with Ar, He, and H₂ as collision partners, while the Landau–Teller model predicted a slower vibrational relaxation process than the measured data. Modifications were applied to the Millikan–White relaxation data of the CO–Ar and CO–H₂ systems, and the predictions based on the Landau–Teller model and modified parameters agreed well with the measured vibrational temperature and vibrational relaxation data.

In addition, the measured and calculated vibrational temperature behind incident shock waves were compared to highlight the necessity of coordinate conversion for vibrational temperature calculations in complex flows. Moreover, the acceleration effects of H₂O on the vibrational relaxation process of CO were primarily shown by comparing the measured vibrational temperature from test gases with different purities. Finally, the detailed vibrational distribution functions of CO were obtained from the StS calculations, and the nonequilibrium distributions were found at the early stage of vibrational relaxation for the studied mixtures, with the higher vibrational levels of CO significantly larger than the corresponding Boltzmann distribution. It should be noted that chemical reactions are not considered in the present StS kinetics. This limitation stems from the fact that the experiments reported in Table I only extend up to 2820 K, so the present study focuses on pure vibrational relaxation. Work is in progress on doing higher temperature shock-tube experiments and developing StS kinetics that incorporate the consideration of very high vibrational states of CO and chemical reactions.

SUPPLEMENTARY MATERIAL

Supplementary material S1 includes the new datasets of vibrational StS rate coefficients of the collision between CO and additives

calculated using the mixed Quantum-Classical method and the FHO model. Supplementary material S2 includes detailed information (including the fill gas pressure and temperature in the low-pressure driven section, velocity of the incident and reflected shocks, velocity of the gas behind the incident shocks, and raw data of the measured pressure, rotational temperature, and vibrational temperature) of all the experiments.

ACKNOWLEDGMENTS

This study was supported by the frontier scientific research program of Deep Space Exploration Laboratory (Grant No. 2022-QYKYJH-HXYF-019), the National Natural Science Foundation of China (Grant Nos. 12027801 and 12302391), and the China Postdoctoral Science Foundation (Grant Nos. 2021M703084 and 2022M723233). The authors would like to thank Dr. Franck Thibault for sharing their PES code of the CO–Ar system.

AUTHOR DECLARATIONS

Conflict of Interest

The authors have no conflicts to disclose.

Author Contributions

D.H. and Q.H. contributed equally to this paper.

Dong He: Conceptualization (equal); Data curation (equal); Formal analysis (equal); Investigation (equal); Methodology (equal); Writing – original draft (equal). **Qizhen Hong:** Conceptualization (equal); Data curation (equal); Formal analysis (equal); Investigation (equal); Methodology (equal); Writing – original draft (equal). **Fei Li:** Project administration (equal); Resources (equal); Supervision (equal); Writing – review & editing (equal). **Quanhua Sun:** Formal analysis (equal); Supervision (equal); Validation (equal); Writing – review & editing (equal). **Ting Si:** Funding acquisition (equal); Project administration (equal); Supervision (equal); Validation (equal); Writing – review & editing (equal). **Xisheng Luo:** Funding acquisition (equal); Project administration (equal); Supervision (equal); Visualization (equal); Writing – review & editing (equal).

DATA AVAILABILITY

The data that supports the findings of this study are available within the supplementary material.

REFERENCES

- ¹H. Koo, V. Raman, and P. L. Varghese, “Direct numerical simulation of supersonic combustion with thermal nonequilibrium,” *Proc. Combust. Inst.* **35**, 2145 (2015).
- ²R. Fiévet, S. Voelkel, H. Koo, V. Raman, and P. L. Varghese, “Effect of thermal nonequilibrium on ignition in scramjet combustors,” *Proc. Combust. Inst.* **36**, 2901 (2017).
- ³C. Johnston, A. Brandis, and K. Sutton, “Shock layer radiation modeling and uncertainty for Mars entry,” in *43rd AIAA Thermophysics Conference* (American Institute of Aeronautics and Astronautics, 2012).
- ⁴B. A. Cruden, D. Prabhu, and R. Martinez, “Absolute radiation measurement in Venus and Mars entry conditions,” *J. Spacecr. Rockets* **49**, 1069 (2012).

- ⁵A. M. Brandis, C. O. Johnston, B. A. Cruden, D. K. Prabhu, A. A. Wray, Y. Liu, D. W. Schwenke, and D. Bose, "Validation of CO 4th positive radiation for Mars entry," *J. Quant. Spectrosc. Radiat. Transfer* **121**, 91 (2013).
- ⁶C. O. Johnston and A. M. Brandis, "Modeling of nonequilibrium CO Fourth-Positive and CN Violet emission in CO₂-N₂ gases," *J. Quant. Spectrosc. Radiat. Transfer* **149**, 303 (2014).
- ⁷B. A. Cruden, A. M. Brandis, and M. E. MacDonald, "Characterization of CO thermochemistry in incident shockwaves," in *2018 Joint Thermophysics and Heat Transfer Conference* (American Institute of Aeronautics and Astronautics, 2018).
- ⁸D. He, L. Shi, D. Nativel, J. Herzler, M. Fikri, and C. Schulz, "CO-concentration and temperature measurements in reacting CH₄/O₂ mixtures doped with diethyl ether behind reflected shock waves," *Combust. Flame* **216**, 194 (2020).
- ⁹D. He, D. Nativel, J. Herzler, J. B. Jeffries, M. Fikri, and C. Schulz, "Laser-based CO concentration and temperature measurements in high-pressure shock-tube studies of n-heptane partial oxidation," *Appl. Phys. B* **126**, 142 (2020).
- ¹⁰M. Pelucchi, C. Cavallotti, T. Faravelli, and S. J. Klippenstein, "H-Abstraction reactions by OH, HO₂, O, O₂ and benzyl radical addition to O₂ and their implications for kinetic modelling of toluene oxidation," *Phys. Chem. Chem. Phys.* **20**, 10607 (2018).
- ¹¹V. Blackman, "Vibrational relaxation in oxygen and nitrogen," *J. Fluid Mech.* **1**, 61 (1956).
- ¹²W. J. Hooker and R. C. Millikan, "Shock-tube study of vibrational relaxation in carbon monoxide for the fundamental and first overtone," *J. Chem. Phys.* **38**, 214 (1963).
- ¹³D. L. Matthews, "Vibrational relaxation of carbon monoxide in the shock tube," *J. Chem. Phys.* **34**, 639 (1961).
- ¹⁴R. C. Millikan, "Carbon monoxide vibrational relaxation in mixtures with helium, neon, and krypton," *J. Chem. Phys.* **40**, 2594 (1964).
- ¹⁵R. C. Millikan and D. R. White, "Vibrational energy exchange between N₂ and CO. The vibrational relaxation of nitrogen," *J. Chem. Phys.* **39**, 98 (1963).
- ¹⁶D. R. White and R. C. Millikan, "Vibrational relaxation in air," *AIAA J.* **2**, 1844 (1964).
- ¹⁷C. J. S. M. Simpson, T. R. D. Chandler, and R. E. Richards, "A shock tube study of vibrational relaxation in pure CO₂ and mixtures of CO₂ with the inert gases, nitrogen, deuterium and hydrogen," *Proc. R. Soc. London, Ser. A* **317**, 265 (1970).
- ¹⁸R. C. Millikan and D. R. White, "Systematics of vibrational relaxation," *J. Chem. Phys.* **39**, 3209 (1963).
- ¹⁹S. J. Lukasik and J. E. Young, "Vibrational relaxation times in nitrogen," *J. Chem. Phys.* **27**, 1149 (1957).
- ²⁰A. R. Fairbairn and A. G. Gaydon, "The dissociation of carbon monoxide," *Proc. R. Soc. London, Ser. A* **312**, 207 (1969).
- ²¹J. P. Appleton, M. Steinberg, and D. J. Liguornik, "Shock-tube study of carbon monoxide dissociation using vacuum-ultraviolet absorption," *J. Chem. Phys.* **52**, 2205 (1970).
- ²²R. K. Hanson, "Shock-tube study of carbon monoxide dissociation kinetics," *J. Chem. Phys.* **60**, 4970 (1974).
- ²³H.-J. Mick, M. Burmeister, and P. Roth, "Atomic resonance absorption spectroscopy measurements on high-temperature CO dissociation kinetics," *AIAA J.* **31**, 671 (1993).
- ²⁴R. K. Hanson and D. F. Davidson, "Recent advances in laser absorption and shock tube methods for studies of combustion chemistry," *Prog. Energy Combust. Sci.* **44**, 103 (2014).
- ²⁵C. S. Goldenstein, R. M. Spearrin, J. B. Jeffries, and R. K. Hanson, "Infrared laser-absorption sensing for combustion gases," *Prog. Energy Combust. Sci.* **60**, 132 (2017).
- ²⁶I. Stranic, S. H. Pyun, D. F. Davidson, and R. K. Hanson, "Multi-species measurements in 2-butanol and *i*-butanol pyrolysis behind reflected shock waves," *Combust. Flame* **160**, 1012 (2013).
- ²⁷S. H. Pyun, W. Ren, K.-Y. Lam, D. F. Davidson, and R. K. Hanson, "Shock tube measurements of methane, ethylene and carbon monoxide time-histories in DME pyrolysis," *Combust. Flame* **160**, 747 (2013).
- ²⁸D. He, D. Zheng, Y. Du, J. Li, Y. Ding, and Z. Peng, "Laser-absorption-spectroscopy-based temperature and NH₃-concentration time-history measurements during the oxidation processes of the shock-heated reacting NH₃/H₂ mixtures," *Combust. Flame* **245**, 112349 (2022).
- ²⁹D. Zheng, D. He, Q.-D. Wang, Y. Ding, and Z. Peng, "Simultaneous measurements of temperature, CO, and CO₂ time-history in reacting *n*-heptane/O₂/argon mixtures blended with diethyl ether behind reflected shock waves," *Combust. Flame* **241**, 112057 (2022).
- ³⁰D. He, T. Si, F. Li, and X. Luo, "Development of interference-free rotational and vibrational thermometry for studies on shock-heated thermochemical nonequilibrium CO," *Meas. Sci. Technol.* **34**, 125502 (2023).
- ³¹C. C. Jelloian, F. A. Bendana, C. Wei, R. M. Spearrin, and M. E. MacDonald, "Nonequilibrium vibrational, rotational, and translational thermometry via megahertz laser absorption of CO," *J. Thermophys. Heat Transfer* **36**, 266 (2021).
- ³²C. C. Jelloian, N. Q. Minesi, and R. M. Spearrin, "High-speed mid-infrared laser absorption spectroscopy of CO₂ for shock-induced thermal non-equilibrium studies of planetary entry," *Appl. Phys. B* **128**, 216 (2022).
- ³³J. W. Streicher, A. Krish, and R. K. Hanson, "Vibrational relaxation time measurements in shock-heated oxygen and air from 2000 K to 9000 K using ultraviolet laser absorption," *Phys. Fluids* **32**, 086101 (2020).
- ³⁴A. Krish, J. W. Streicher, and R. K. Hanson, "Spectrally-resolved ultraviolet absorption measurements of shock-heated NO from 2000 K to 6000 K for the development of a two-color rotational temperature diagnostic," *J. Quant. Spectrosc. Radiat. Transfer* **280**, 108073 (2022).
- ³⁵P. M. Finch, J. Girard, C. Strand, W. Yu, J. Austin, H. Hornung, and R. Hanson, "Measurements of time-resolved air freestream nitric oxide rotational, vibrational temperature and concentration in the T5 reflected shock tunnel," in *AIAA Propulsion And Energy 2020 Forum* (American Institute of Aeronautics and Astronautics, 2020).
- ³⁶M. F. Campbell, T. Parise, A. M. Tulgestke, R. M. Spearrin, D. F. Davidson, and R. K. Hanson, "Strategies for obtaining long constant-pressure test times in shock tubes," *Shock Waves* **25**, 651 (2015).
- ³⁷D. He, Y. Ding, L. Shi, D. Zheng, and Z. Peng, "Simultaneous temperature and CO-concentration time-history measurements during the pyrolysis and ultra-fuel-rich oxidation of ethanol, diethyl ether, n-heptane, and isooctane behind reflected shock waves," *Combust. Flame* **232**, 111537 (2021).
- ³⁸D. I. Pineda, F. A. Bendana, and R. Mitchell Spearrin, "Competitive oxidation of methane and C₂ hydrocarbons discerned by isotopic labeling and laser absorption spectroscopy of CO isotopologues in shock-heated mixtures," *Combust. Flame* **224**, 54 (2021).
- ³⁹C. Park, *Nonequilibrium Hypersonic Aerothermodynamics* (Wiley, New York, 1990).
- ⁴⁰L. Landau and E. Teller, "On the theory of sound dispersion," *Phys. Z. Sowjetunion* **10**, 34 (1936).
- ⁴¹J. D. Anderson, *Hypersonic and High-Temperature Gas Dynamics*, 3rd ed. (American Institute of Aeronautics and Astronautics, Inc., Washington, DC, 2019).
- ⁴²E. Nagnibeda and E. Kustova, *Non-equilibrium Reacting Gas Flows: Kinetic Theory of Transport and Relaxation Processes* (Springer, Berlin, 2009).
- ⁴³M. Panesi, A. Munafò, T. E. Magin, and R. L. Jaffe, "Nonequilibrium shock-heated nitrogen flows using a rovibrational state-to-state method," *Phys. Rev. E* **90**, 013009 (2014).
- ⁴⁴Q. Hong, X. Wang, Y. Hu, and Q. Sun, "Development of a stagnation streamline model for thermochemical nonequilibrium flow," *Phys. Fluids* **32**, 046102 (2020).
- ⁴⁵I. N. Kadochnikov and I. V. Arsentiev, "Modelling of vibrational nonequilibrium effects on the H₂-air mixture ignition under shock wave conditions in the state-to-state and mode approximations," *Shock Waves* **30**, 491 (2020).
- ⁴⁶I. N. Kadochnikov, I. V. Arsentiev, B. I. Loukhovitski, and A. S. Sharipov, "State-to-state vibrational kinetics of diatomic molecules in laser-induced ignition of a syngas-air mixture: Modeling study," *Chem. Phys.* **562**, 111669 (2022).
- ⁴⁷R. N. Schwartz, Z. I. Slawsky, and K. F. Herzfeld, "Calculation of vibrational relaxation times in gases," *J. Chem. Phys.* **20**, 1591 (2004).
- ⁴⁸I. V. Adamovich, S. O. Macheret, J. W. Rich, and C. E. Treanor, "Vibrational relaxation and dissociation behind shock waves. Part 1—Kinetic rate models," *AIAA J.* **33**, 1064 (1995).
- ⁴⁹D. A. Andrienko and I. D. Boyd, "State-specific dissociation in O₂-O₂ collisions by quasiclassical trajectory method," *Chem. Phys.* **491**, 74 (2017).

- ⁵⁰Q. Hong, M. Bartolomei, C. Coletti, A. Lombardi, Q. Sun, and F. Pirani, "Vibrational energy transfer in CO + N₂ collisions: A database for V-V and V-T/R quantum-classical rate coefficients," *Molecules* **26**, 7152 (2021).
- ⁵¹X. Wang, Q. Hong, C. Yang, and Q. Sun, "Uncertainty quantification in state-specific modeling of thermal relaxation and dissociation of oxygen," *AIAA J.* **61**, 2734 (2023).
- ⁵²G. Colonna, M. Tuttafesta, M. Capitelli, and D. Giordano, "Non-arrhenius NO formation rate in one-dimensional nozzle airflow," *J. Thermophys. Heat Transfer* **13**, 372 (1999).
- ⁵³M. Capitelli, R. Celiberto, G. Colonna, F. Esposito, C. Gorse, K. Hassouni, A. Laricchiuta, and S. Longo, in *Fundamental Aspects of Plasma Chemical Physics: Kinetics*, Series on Atomic, Optical, and Plasma Physics (Springer, 2016), Vol. 85.
- ⁵⁴S. F. Gimelshein, I. J. Wysong, A. J. Fangman, D. A. Andrienko, O. V. Kunova, E. V. Kustova, C. Garbacz, M. Fossati, and K. Hanquist, "Kinetic and continuum modeling of high-temperature oxygen and nitrogen binary mixtures," *J. Thermophys. Heat Transfer* **36**, 399 (2022).
- ⁵⁵S. F. Gimelshein, I. J. Wysong, A. J. Fangman, D. A. Andrienko, O. V. Kunova, E. V. Kustova, F. Morgado, C. Garbacz, M. Fossati, and K. M. Hanquist, "Kinetic and continuum modeling of high-temperature air relaxation," *J. Thermophys. Heat Transfer* **36**, 870 (2022).
- ⁵⁶L. D. Pietanza, G. Colonna, and M. Capitelli, "Non-equilibrium plasma kinetics of reacting CO: An improved state to state approach," *Plasma Sources Sci. Technol.* **26**, 125007 (2017).
- ⁵⁷L. D. Pietanza, G. Colonna, A. Laricchiuta, and M. Capitelli, "Non-equilibrium electron and vibrational distributions under nanosecond repetitively pulsed CO discharges and afterglows: II. The role of radiative and quenching processes," *Plasma Sources Sci. Technol.* **27**, 095003 (2018).
- ⁵⁸A. Aliat, A. Chikhaoui, and E. V. Kustova, "Nonequilibrium kinetics of a radiative CO flow behind a shock wave," *Phys. Rev. E* **68**, 056306 (2003).
- ⁵⁹A. Aliat, E. V. Kustova, and A. Chikhaoui, "State-to-state reaction rates in gases with vibration-electronic-dissociation coupling: The influence on a radiative shock heated CO flow," *Chem. Phys.* **314**, 37 (2005).
- ⁶⁰F. Bonelli, M. Tuttafesta, G. Colonna, L. Cutrone, and G. Pascasio, "An MPI-CUDA approach for hypersonic flows with detailed state-to-state air kinetics using a GPU cluster," *Comput. Phys. Commun.* **219**, 178 (2017).
- ⁶¹X. Wang, J. Guo, Q. Hong, and S. Li, "High-fidelity state-to-state modeling of hypersonic flow over a double cone," *Phys. Fluids* **35**, 116101 (2023).
- ⁶²D. He, T. Si, M. Fikri, and X. Luo, "Interference-free laser-based temperature and CO-concentration measurements for shock-heated isoctane and isoctane/ethanol blends," *Meas. Sci. Technol.* **35**, 015502 (2024).
- ⁶³C. W. vonRosenberg, K. N. C. Bray, and N. H. Pratt, "The effect of water vapor on the vibrational relaxation of CO," *Symp. (Int.) Combust.* **13**, 89 (1971).
- ⁶⁴L. S. Rothman, I. E. Gordon, R. J. Barber, H. Dothe, R. R. Gamache, A. Goldman, V. I. Perevalov, S. A. Tashkun, and J. Tennyson, "HITEMP, the high-temperature molecular spectroscopic database," *J. Quant. Spectrosc. Radiat. Transfer* **111**, 2139 (2010).
- ⁶⁵I. E. Gordon, L. S. Rothman, R. J. Hargreaves, R. Hashemi, E. V. Karlovets, F. M. Skinner, E. K. Conway, C. Hill, R. V. Kochanov, Y. Tan, P. Wcislo, A. A. Finenko, K. Nelson, P. F. Bernath, M. Birk, V. Boudon, A. Campargue, K. V. Chance, A. Coustenis, B. J. Drouin, J. M. Flaud, R. R. Gamache, J. T. Hodges, D. Jacquemart, E. J. Mlawer, A. V. Nikitin, V. I. Perevalov, M. Rotger, J. Tennyson, G. C. Toon, H. Tran, V. G. Tyuterev, E. M. Adkins, A. Baker, A. Barbe, E. Canè, A. G. Császár, A. Dudaryonok, O. Egorov, A. J. Fleisher, H. Fleurbaey, A. Foltynowicz, T. Furtenbacher, J. J. Harrison, J. M. Hartmann, V. M. Horneman, X. Huang, T. Karman, J. Karns, S. Kassi, I. Kleiner, V. Kofman, F. Kwabia-Tchana, N. N. Lavrentieva, T. J. Lee, D. A. Long, A. A. Lukashchik, O. M. Lyulin, V. Y. Makhnev, W. Matt, S. T. Massie, M. Melosso, S. N. Mikhailenko, D. Mondelain, H. S. P. Müller, O. V. Naumenko, A. Perrin, O. L. Polyansky, E. Raddaoui, P. L. Raston, Z. D. Reed, M. Rey, C. Richard, R. Tóbiás, I. Sadiek, D. W. Schwenke, E. Starikova, K. Sung, F. Tamassia, S. A. Tashkun, J. Vander Auwera, I. A. Vasilenko, A. A. Viganin, G. L. Villanueva, B. Vispoel, G. Wagner, A. Yachmenev, and S. N. Yurchenko, "The HITRAN2020 molecular spectroscopic database," *J. Quant. Spectrosc. Radiat. Transfer* **277**, 107949 (2022).
- ⁶⁶G. D. Billing, "Rate constants and cross sections for vibrational transitions in atom-diatom and diatom-diatom collisions," *Comput. Phys. Commun.* **32**, 45 (1984).
- ⁶⁷Q. Hong, M. Bartolomei, F. Esposito, C. Coletti, Q. Sun, and F. Pirani, "Reconciling experimental and theoretical vibrational deactivation in low-energy O + N₂ collisions," *Phys. Chem. Chem. Phys.* **23**, 15475 (2021).
- ⁶⁸Q. Hong, M. Bartolomei, F. Pirani, F. Esposito, Q. Sun, and C. Coletti, "Vibrational deactivation in O(³P) + N₂ collisions: From an old problem towards its solution," *Plasma Sources Sci. Technol.* **31**, 084008 (2022).
- ⁶⁹G. C. McBane, "A three-dimensional He-CO potential energy surface with improved long-range behavior," *J. Mol. Spectrosc.* **330**, 211 (2016).
- ⁷⁰C. T. Wickham-Jones, H. T. Williams, and C. J. S. M. Simpson, "Experimental and theoretical studies of CO vibrational relaxation by He atoms," *J. Chem. Phys.* **87**, 5294 (1987).
- ⁷¹M. L. da Silva, V. Guerra, and J. Loureiro, "State-resolved dissociation rates for extremely nonequilibrium atmospheric entries," *J. Thermophys. Heat Transfer* **21**, 40 (2007).
- ⁷²Y. Sumiyoshi and Y. Endo, "Three-dimensional potential energy surface of Ar-CO," *J. Chem. Phys.* **142**, 024314 (2015).
- ⁷³G. Kowzan, P. Wcislo, M. Słowiński, P. Masłowski, A. Viel, and F. Thibault, "Fully quantum calculations of the line-shape parameters for the Hartmann-Tran profile: A CO-Ar case study," *J. Quant. Spectrosc. Radiat. Transfer* **243**, 106803 (2020).
- ⁷⁴O. Denis-Alpizar, R. J. Bemish, and M. Meuwly, "Communication: Vibrational relaxation of CO(¹Σ) in collision with Ar(¹S) at temperatures relevant to the hypersonic flight regime," *J. Chem. Phys.* **146**, 111102 (2017).
- ⁷⁵J. Chen, J. Li, J. M. Bowman, and H. Guo, "Energy transfer between vibrationally excited carbon monoxide based on a highly accurate six-dimensional potential energy surface," *J. Chem. Phys.* **153**, 054310 (2020).
- ⁷⁶M. A. Kovacs and M. E. Mack, "Vibrational relaxation measurements using "Transient" stimulated Raman scattering," *Appl. Phys. Lett.* **20**, 487 (2003).
- ⁷⁷Q. Hong, L. Storch, M. Bartolomei, F. Pirani, Q. Sun, and C. Coletti, "Inelastic N₂ + H₂ collisions and quantum-classical rate coefficients: Large datasets and machine learning predictions," *Eur. Phys. J. D* **77**, 128 (2023).
- ⁷⁸L. F. Shampine and M. W. Reichelt, "The MATLAB ODE suite," *SIAM J. Sci. Comput.* **18**, 1 (1997).
- ⁷⁹H. W. Coleman and W. G. Steele, *Experimentation, Validation, and Uncertainty Analysis for Engineers*, 3rd ed. (John Wiley and Sons, Inc., Hoboken, NJ, 2009).
- ⁸⁰L. Lotte Poulsen and G. D. Billing, "Vibrational deactivation of CO($v = 1$) by p-H₂ and o-H₂," *Chem. Phys.* **73**, 313 (1982).